

# Mechanism design for walking typed solar panel-cleaning robot using triple driving lines

Woo Jin Jang<sup>1</sup>, Jin Gahk Kim<sup>2</sup>, Sang Hun Lee<sup>2</sup>, Dong Hwan Kim<sup>3</sup>

<sup>1</sup>Equipment Technology Research Center, Samsung Electronics, Suwon, Korea

<sup>2</sup>Department of Robotics, Seoul National University of Science and Technology, Seoul, Korea

<sup>3</sup>Department of Mechanical Design and Robot Engineering, Seoul National University of Science and Technology, Seoul, Korea

## Article Info

### Article history:

Received Aug 18, 2021

Revised Dec 24, 2021

Accepted Jan 10, 2022

### Keywords:

Driving lines

Linkage mechanism

Solar panel-cleaning robot

Vacuum pads

Walking typed robot

## ABSTRACT

In this study, we propose a walking-type solar power cleaning robot mechanism driven by a driving unit composed of three driving lines. The triple driving lines are driven using a link mechanism, and vacuum pads are attached to each driving line to move the robot body through a sequence operation between the three lines. Through this mechanism, the robot body can be moved horizontally with the panel without folding the pad, and the amount of vertical movement is minimized during movement. By analyzing the pressure patterns of the pads on the driving line, smooth and fast movement was possible.

*This is an open access article under the [CC BY-SA](#) license.*



## Corresponding Author:

Dong Hwan Kim

Department of Mechanical Design and Robot Engineering, Seoul National University of Science and Technology

Seoul, Korea

Email: ziyad.allawi@gmail.com

## 1. INTRODUCTION

Today, as the demand for solar energy is increasing, the solar market is expanding both domestically and abroad [1]–[4]. Also, as the solar panel installation cost is gradually reduced, the demand for solar panel for home is also increasing. As the demand for home solar panels increases, regular maintenance is also becoming more important. Industrial photovoltaic panels installed in large-scale complexes that produce a large amount of energy use large-scale moving devices to clean solar panels, but relatively small-scale photovoltaic panels are maintained and cleaned with robot-type cleaning devices. Large-scale industrial photovoltaic panels use rail-type photovoltaic panel-cleaning robots for management, but manpower must be used to clean relatively small panels [5]–[8]. This issue causes considerable economic burden and safety problems. In order to solve this problem, it is necessary to develop an autonomous mobile solar panel-cleaning robot that can easily clean small-scale solar panels [9]–[11].

In order to manufacture a robot capable of running on a panel with a maximum inclination angle of 40 degrees, a walking-driving unit was devised that improved the driving problems of the existing mobile solar panel-cleaning robot. In general, if wheels or caterpillars are used without using a suction pad, it is difficult to drive a high-inclined panel [12]–[15]. On the other hand, when a caterpillar-type [16]–[18] driving part using suction pads is used, sometimes slippage occurs due to the folding of the pad [19]–[22].

In this study, we propose a driving module that can drive high-inclined panels and minimize pad folding. Additionally, a new driving unit design method that can increase the moving speed of the walking type solar panel-cleaning robot is proposed, and an adsorption mechanism according to the triple driving unit structure is proposed. The designed walking robot is manufactured and tested to verify its performance.

## 2. MECHANISM DESIGN

### 2.1. Linkage mechanism

Before manufacturing a walking type-driving unit, a driving mechanism having two conditions must be configured. First, when the robot moves, the vertical movement of the body should be minimized because it is possible to acquire stable signals from sensors and cameras used in the robot for autonomous driving and location recognition. Second, when the vacuum suction pads used for driving the inclined panel are attached to and detached from the panel, the pad surface should move as parallel to the panel surface as possible so that the pad unfolds. A drive module with linkage mechanism that satisfies these two conditions was devised.

Figure 1 shows the configuration of the link driving module using RecurDyn [23]. A module uses 25 links, and Links 1, 2, and 4 have the same length. When Links 1 and 4 rotate at the same speed in opposite directions, they have a path locus drawn by the end point of the pad. Drawing the locus [24], [25] the linkage mechanism is constructed. After the pad starts adsorption on the floor, it moves forward by pulling the robot body along the path the pad moves, which is like riding an ice sled. At first, the length of Link 1, 2, and 4 was designated as 30 mm so that the robot could move 60 mm in one step. When Link 5 shown in Figure 1 is not fixed the robot that uses this link mechanism is likely to slide down on a slope. In order to prevent the robot from sagging backward while moving on a slope, Link 5 of each module is connected together with one additional link.

Here, as shown in Figure 2, one configuration that connects two modules is called a driving line. The lower drawing of Figure 2 shows the driving line composed of links as shown in the upper one and the driving line is reconstructed using gears. Links 1 and 4 were replaced with spur gears, and four spur gears were rotated through one driving gear to move the link.

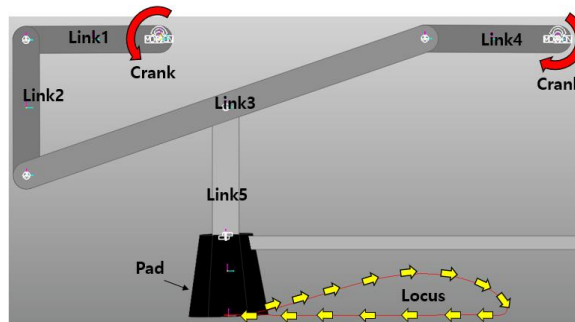


Figure 1. Linkage mechanism with 5 links

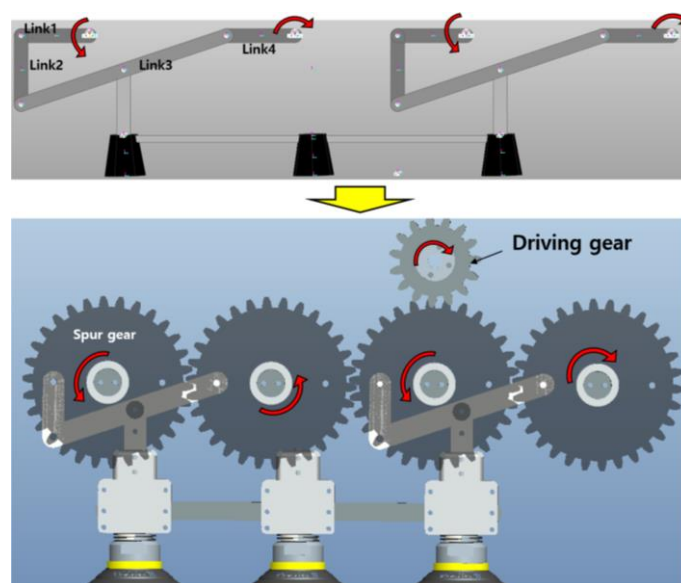


Figure 2. Mechanism design of driving line

## 2.2. Double driving line structure

The driving units at both ends of the robot were constructed using the designed driving lines. The upper left one in Figure 3 is a structure with two driving lines per driving unit. In the lower left figure, the first and second driving line consist of one driving unit that drives one leg of the robot. When the driving motor rotates, the spur gears of each driving line rotates to rotate the links. As shown on the right of Figure 3, the spur gears constituting the driving line are connected to each other, and thus, a total of 8 spur gears forming a double driving line are rotated from the gear of one driving motor.

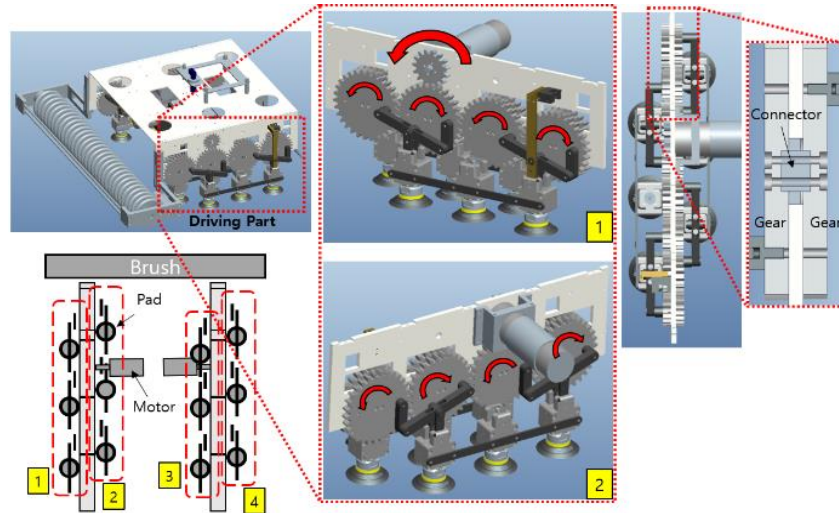


Figure 3. Configuration of driving unit composed of double driving lines

Figure 4 shows the movement of the pads of the driving lines when the robot moves forward. Among the two driving lines constituting one leg of the robot, when the spur gears of the driving line in the first column rotate by  $0^\circ \leq \theta \leq 180^\circ$ , the pads of the corresponding line lift up. At this time, the pads connected to the inner driving line 2 are attached to the panel and pull the robot body, so that the robot body moves forward. The other leg on the opposite side of the robot also synchronizes with one leg and performs the same motion, and as a result, the forward motion of the robot body is completed.

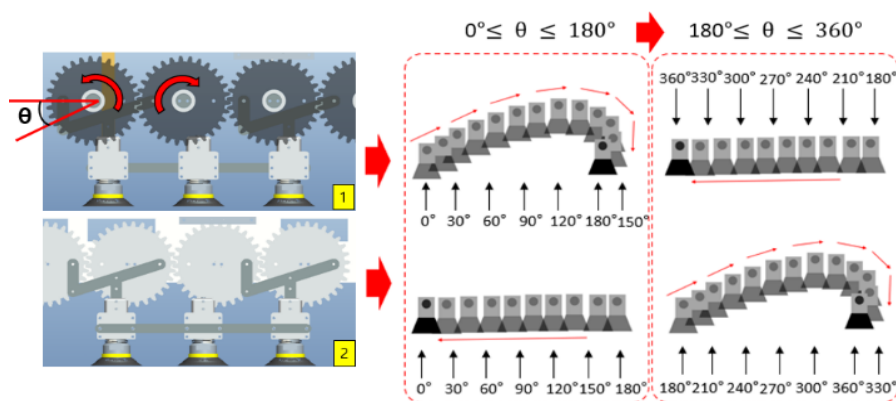


Figure 4. Suction pad movement path

Next, when the spur gear rotates at an angle of  $180^\circ \leq \theta \leq 360^\circ$ , the pads of the first driving line are attached to the panel and move forward by pulling the body. And the pads on the 2<sup>nd</sup> driving line are stepping up. The robot moves while repeating this process.

Figure 5 is the configuration diagram of the driving line where the vacuum pump and the solenoid valve are connected. The 1<sup>st</sup> and 3<sup>rd</sup> driving lines are connected to the 2<sup>nd</sup>, 4<sup>th</sup>, and 6<sup>th</sup> solenoid valves, and the

2<sup>nd</sup> and 4<sup>th</sup> driving lines are connected to the 1<sup>st</sup>, 3<sup>rd</sup>, and 5<sup>th</sup> solenoid valves. And the 7<sup>th</sup> solenoid valve is connected to the body-rotating unit.

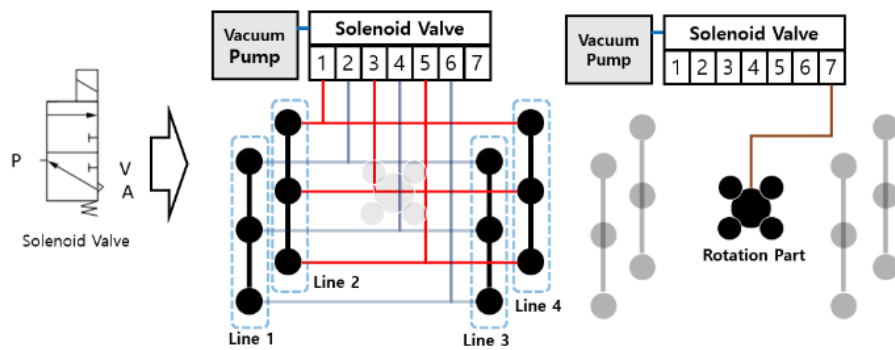


Figure 5. Configuration of driving and rotating part with 3-way solenoid valves

Figure 6 is a diagram explaining the driving process associated with the solenoid valves. At first, the 2<sup>nd</sup> and 4<sup>th</sup> driving line pads marked in red are in a vacuum state and attached to the panel, and the 1<sup>st</sup> and 3<sup>rd</sup> driving line pads marked in blue are in the atmospheric pressure state. Figure 6 shows the process of lifting up the pads when the spur gear rotates from 0 to 180 degrees.

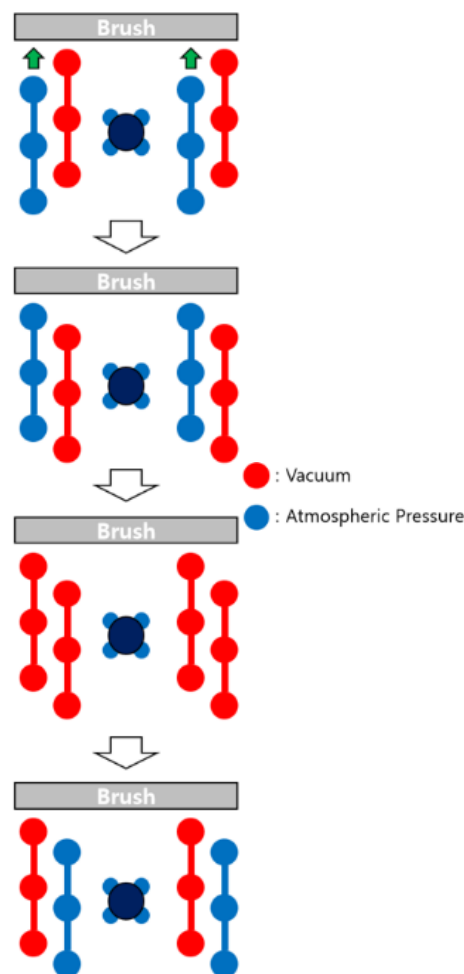


Figure 6. The whole robot driving process

At this time, after the lifted-up 1<sup>st</sup> and 3<sup>rd</sup> driving line pads are attached to the panel again, the 2<sup>nd</sup> and 4<sup>th</sup> driving line pads that were in a vacuum state do not immediately change to atmospheric pressure. It takes a little time for each pad to enter a complete vacuum state or change to atmospheric pressure. If this time is not taken into account, the robot will fall due to the low vacuum pressure of the pads. After making the entire pad under vacuum pressure, the driving line pads to be lifted up are changed to atmospheric pressure before moving forward again.

However, some problems occur when driving in the sequence shown in Figure 6. First, as seen in Figure 7, there is a delay period until the entire driving line pad becomes vacuum pressure. The moving speed of the robot reduces inevitably by this section. Second, as seen in Figure 8, if the robot moves 60 mm in one step, the body advances only by 60 mm. Although one cycle consists of two steps, the amount of movement per cycle of the robot is equal to that of one step, so the amount of movement of the robot is not as large as expected. Third, in the case of driving as shown in Figure 6, since the motors at both ends cannot be controlled respectively, there is a problem that the straight-line correction control is difficult. To solve this problem, a new drive structure is devised [26].

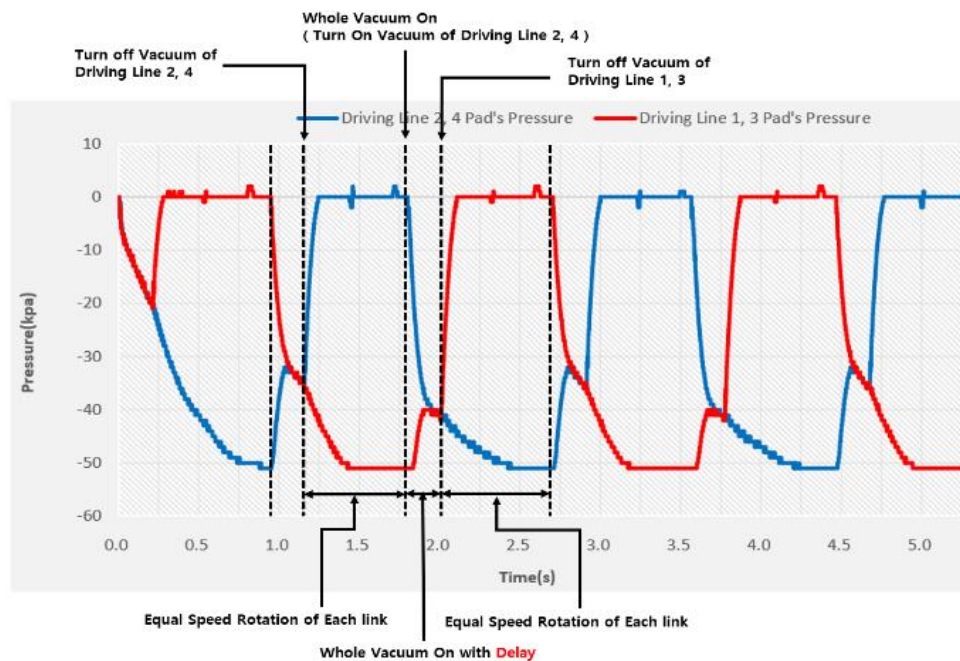


Figure 7. Pressure responses of pads according to driving sequence

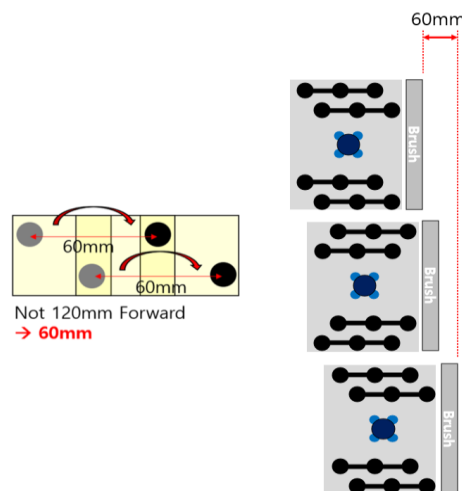


Figure 8. Advance of body per wheel with gear rotation



### 2.3. Triple driving line configuration

Figure 9 is a structure composed of three driving lines per driving unit. A triple driving line structure was proposed by adding one driving line to the double driving line structure. Although the linkage mechanism is applied in the same way as in the double structure, as shown in Figure 10, the driving lines of each row have a phase difference of 120 degrees. By adding a driving line, there is no delay period in each sequence, and the pads can be continuously attached to the panel and move forward.

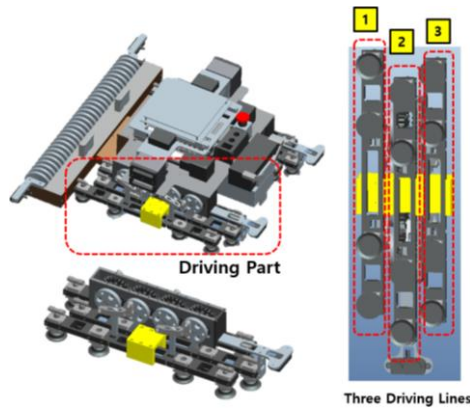


Figure 9. Driving part of three driving lines

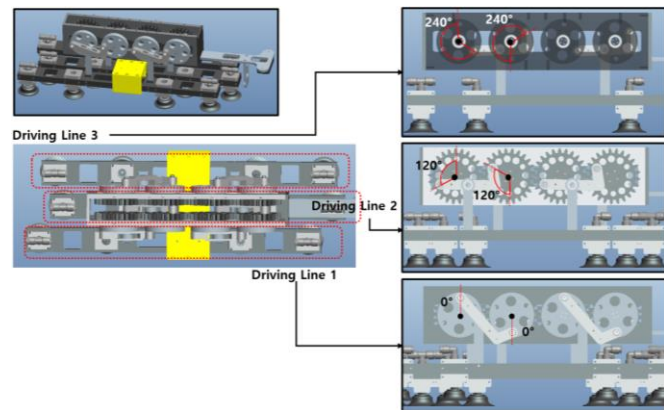


Figure 10. Phase difference between each driving line

Figure 11 shows the results of analysis by RecurDyn to understand the total robot movement amount by checking the forward (x-direction) movement of the driving line pads. The amount of movement in the x-direction was indicated by designating the end point of the pad on the front of each driving line. Here, it is assumed that one rotation of the spur gear (360 degrees) makes is one cycle of movement, and it is assumed that one cycle takes 2 seconds. The part where the pad pressure descends is the process of the robot moving forward with the pads attached to the panel.

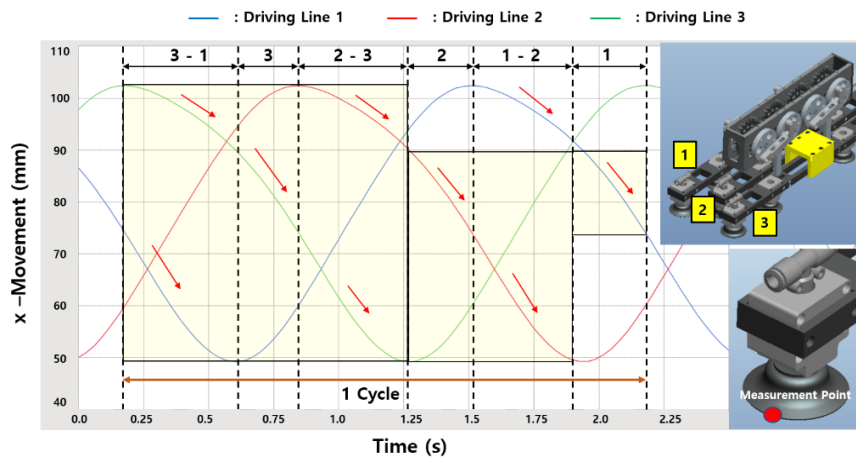


Figure 11. Forward advance of body with three driving lines

From about 0.15 to 0.6 sec, the first and third driving line pads are attached to the panel and the robot body moves forward. From 0.6 to 0.85 sec, 3 driving line pads are attached to the panel, and from 0.85 to 1.25 sec, the 2<sup>nd</sup> and 3<sup>rd</sup> driving line pads are attached to the panel and the robot body moves forward again. From 1.25 to 1.5 sec, only the pads on the driving line 2 are attached to the panel, and from 1.5 to 1.9 sec, the pads on the driving lines 1 and 2 are attached to the panel, then the robot moves forward. Finally, from 1.9 to 2.2 sec, only one driving line pad is attached to the panel, and the robot moves forward again. As you can see from the results, there is always at least one driving line pad attached to the panel. It means that

the delay time that creates a vacuum pressure across the entire pad in the double driving line structure is eliminated in the triple driving lines structure. Furthermore, since the motors at both ends can be controlled individually, straight-line compensation driving is possible. When the lengths of Link 1, 2, and 4 of the double driving line are equally 25 mm, it is expected that the robot advances 50 mm per step. But in the triple driving line structure, as seen from Figure 11, it was confirmed that the robot advances 105 mm per cycle. Therefore, it was possible to significantly increase the running speed of the robot [26].

Figure 12 shows the configuration of mechanical elements for operating the drive unit. The triple driving line driving part was modeled and manufactured using spur gears and links in the same way as the double driving line. When the driving motor rotates, power is transmitted through the second spur gear of the driving unit, and it is also connected to the rest of the spur gears to move the link.

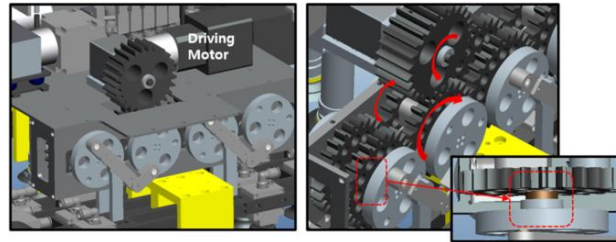


Figure 12. Configuration of mechanical elements to transmit power to the drive unit

Figure 13 is equipped with a driving line guide to prevent the link from shaking. There was a problem that the driving line gradually descended due to the gap of the link while driving. To prevent this gap, an additional guide was inserted to prevent the driving line from being skewed to the left or right.

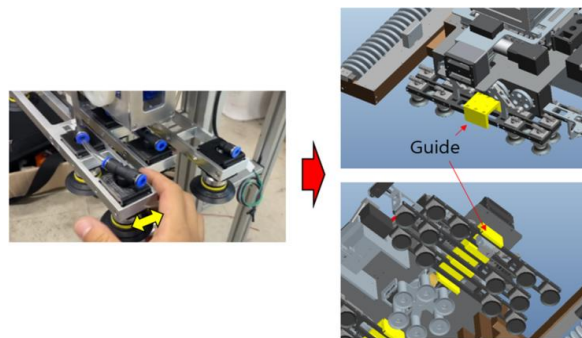


Figure 13 Link's gap prevention guide

#### 2.4. Rotation part design

The robot needs to rotate in place to change direction. When rotating in place, when rotating using the speed difference of the driving part, sliding and large load occurs, so the rotating part that serves as the rotating shaft of the body was designed and manufactured. Figure 14 is a design of a rotating part mounted at the center of the robot. The rotating part composed of 6 pads is initially about 10 mm away from the panel by the compression spring, and then the rotating part is lowered by rotating the cam with a motor. When the vacuum pads of the rotating part are attached to and fixed to the panel under vacuum pressure, both driving parts are driven in opposite directions to rotate in place using the friction of the pads. As a result, the rotating part serves as a rotating shaft and an anti-slip device.

#### 2.5. Vacuum pad selection for driving unit

As the number of driving lines per driving unit increased, the number of mechanical parts also increased. Therefore, it is more prone to slip on the inclined panel due to the increase in the overall weight of the robot. To solve this problem, the number and types of pads was selected for stable driving.

First, the vacuum pad selection condition was derived by expressing the free-body diagram of the robot on the inclined panel, as shown in Figure 15.

$$\mu N + n_{pad} F_h > mg \sin \psi \quad (1)$$

$$N = n_{pad} F_v + mg \cos \psi \quad (2)$$

$$F_v = 2 F_h \quad (3)$$

$$n_{pad} > \frac{mg \sin \psi - \mu mg \cos \psi}{(2\mu + 1) F_h} \quad (4)$$

$$F_h = S P \quad (5)$$

Here,  $n_{pad}$  is the number of pads required and is driven as (4).  $m$  is the robot body weight,  $\psi$  is the panel inclination angle,  $F_v$ , and  $F_h$  are the vertical and horizontal forces to the panel surface due to the vacuum, respectively.  $\mu$  is the friction coefficient between the pad and panel surface. Also,  $S$  is the sectional area of the pad and  $P$  is the vacuum pressure formed inside of the pad.

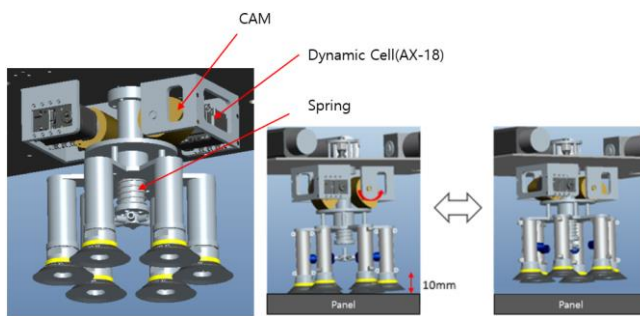


Figure 14. Rotating part design operating with cam

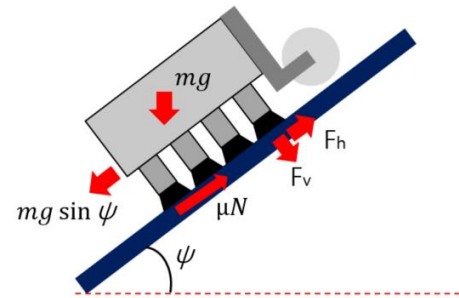


Figure 15. Forces acting to the robot

### 3. MOTION ANALYSIS

#### 3.1. Movement sequence

For inclined panel driving, Figure 16, the vacuum pump and solenoid valve were connected to the triple driving line. Six solenoid valves are used per driving unit, and two pads are connected to one solenoid valve each. And the 7<sup>th</sup> solenoid valve is connected to the pads of the rotating part. When the driving line pad is attached to the panel, the solenoid valve is turned on, and when it is detached from the panel, the solenoid valve is turned off.

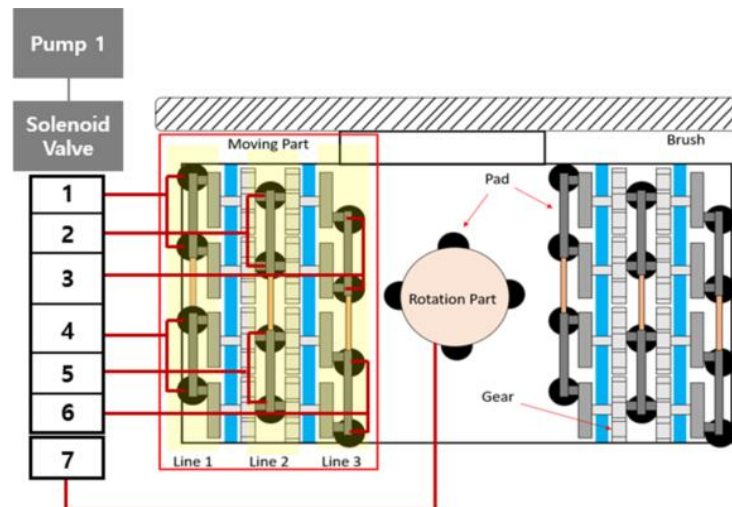


Figure 16. Configuration of driving and rotating part with three driving lines and 3-way solenoid valves



Next, the initialization of robot posture and driving sequence will be described. Figure 17 shows an initialization process performed before driving. When the switch and pump are turned on, shown at Figure 14, the rotating part is lowered from the cam. Then, No. 7 solenoid valve in Figure 16 is turned on, and the rotating pads are in a vacuum pressure state, attached to the panel, thus fixing the robot. After that, the left and right driving units are operated until the pad of the center-driving line from both the left and right driving unit is detected by the proximity sensor as shown in Figure 18. When this task is done, as shown in Figure 16, solenoid valves 1 and 4 are turned on, and solenoid valve 7 is turned off. In this way, the encoder values of the driving motors that operate the left and right driving units of the robot are initialized, thus, from this time the robot is ready to move forward.

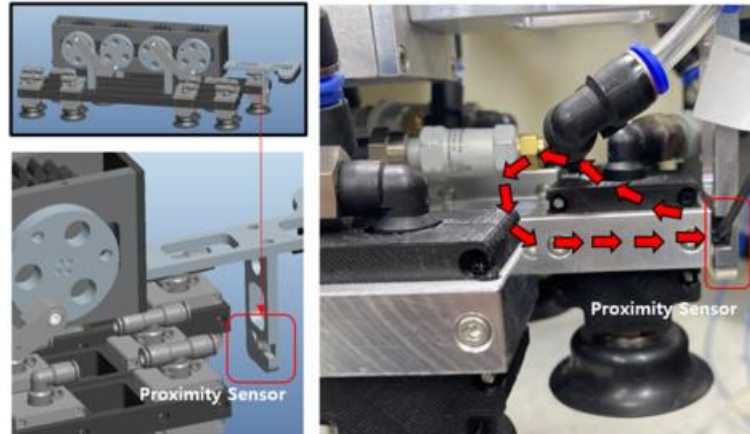
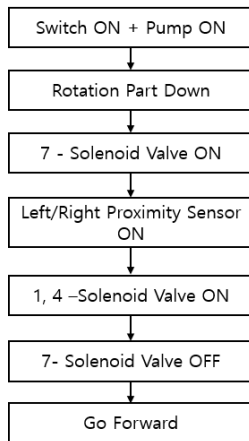


Figure 17. Sequence for initializing the robot

Figure 18. Proximity sensor mounting for robot posture initialization

Figure 19 shows the progress of the robot after the initialization has been completed. When looking at only one driving unit, it was divided into six movements per cycle, and the solenoid valve was controlled to turn on/off according to the encoder value determined according to the rotation angle of the driving unit motor. After the initialization has been completed. As in operation 1 of Figure 19, only the first driving line pads are attached to the panel, and the robot moves forward. Solenoid valves 1 and 4 in Figure 16 are turned on, and the first driving line pads are in a vacuum state, and this state is maintained until operation 2 is made. And in operation 2, solenoid valves 1, 3, 4, and 6 are turned on because the 1<sup>st</sup> and 3<sup>rd</sup> driving line pads are attached to the panel and start moving forward. Two driving line pads are attached and the robot moves forward. From operation 3, the solenoid valve connected to the first driving line turns off, and only driving line 3 is attached to the panel in a vacuum state. In operation 4, driving line 2 pads are additionally attached to the panel, and solenoid valves 2 and 5 are turned on. The robot body moves forward while repeatedly attaching and detaching the pads of drive lines 1, 2, and 3 to the panel.

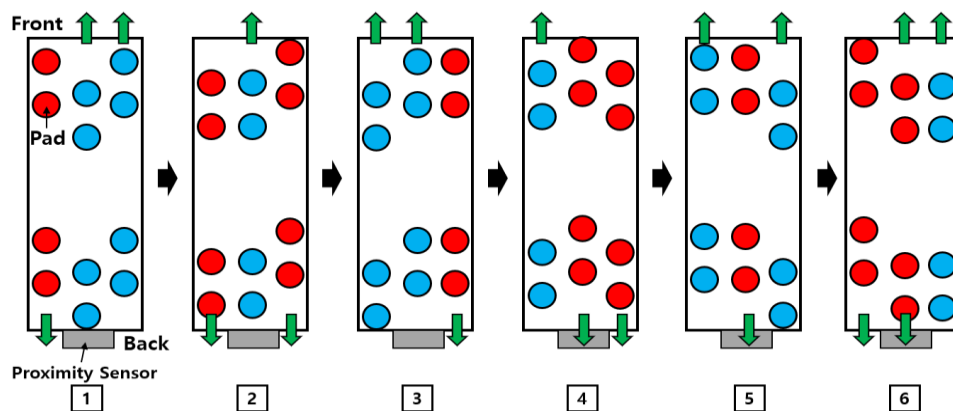


Figure 19. Sequence of triple drive proceeding

### 3.2. Kinematics analysis

A vacuum pump and a solenoid valve were used to drive the solar panel-cleaning robot on the inclined panel. However, if the solenoid valve is not turned on/off at the appropriate encoder value, the pads do not change to atmospheric pressure while the robot is running as shown in Figure 20, so it cannot move forward or slip occurs. As it takes the appropriate time for the corresponding driving line pads to return to full atmospheric pressure it is recommended not to turn off the solenoid valve too soon or too late. Kinematics analysis was conducted to find the solenoid valve control time for stably driving the robot.

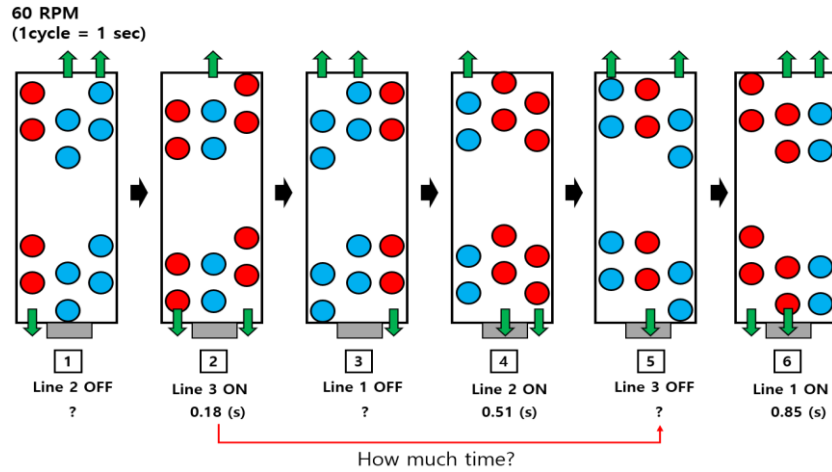


Figure 20. Time control process of solenoid valves

The forces acting on the robot placed on the inclined surface are shown in Figure 21.  $\psi$  is the angle of the inclined panel,  $m$  is the robot weight,  $n_{pad}$  is the number of pads,  $F_v$  is the vertical force of the vacuum pad,  $F_h$  is the horizontal force of the vacuum pad, and  $\mu$  is the vacuum pad friction coefficient. In general, since  $F_v$  has twice the force of  $F_h$ . At this time, when the rotation of the large spur gear is one cycle, the driving force generated when the pad touches the panel and moves the robot forward during one cycle is called  $F$ .  $n$  is the number of pads.

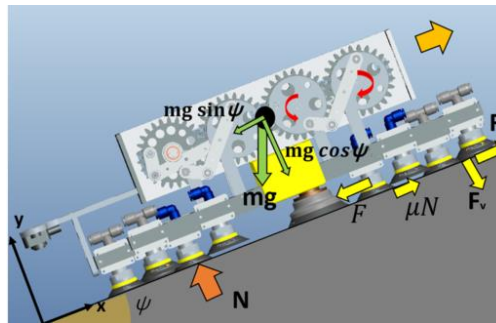


Figure 21. Forces on robot in the inclined panel

$$F_x: -mg \sin \psi + \mu N - F + n F_h = m a_x \quad (6)$$

$$N = n_{pad} F_v + mg \cos \psi \quad (7)$$

$$a_x = -g \sin \psi + g \cos \psi + \left( \frac{2\mu n_{pad}}{m} + \frac{n_{pad}}{m} \right) F_h - \frac{F}{m} \quad (8)$$

The acceleration in the x-axis direction is derived by (8) by arranging (6) and (7). The reason for considering only the x-axis direction as in (8) is that the robot body only moves horizontally without up-and-down movement because the linkage mechanism is applied to the driving unit. Even though  $F_h$  is determined

by (5), P in (5) requires a different pressure pattern for each operation sequence. That is, it is necessary to derive a pressure pattern for each sequence and to control the pads to have this vacuum pressure. Since the magnitude of the driving force changes according to the rotation angle of the driving spur gear, the driving force  $F$  according to the angle must be derived and then substituted into (8).

First, in order to derive the equation for the magnitude of the driving force, the relationship between the rotation angle of the driving motor and the position of the connecting link for one driving module was solved by geometric analysis. At this time, as shown in Figure 22, each parameter value should be derived from the angular change of  $0^\circ \leq \theta \leq 180^\circ$  relative to the red dotted line for each spur gear being in contact each other. This condition is needed because, when rotating at this angle, the pads of each driving line come into contact with the panel, generating maneuverability and increasing driving speed.

$$b = \sqrt{9a^2 - 6a^2 \cos \theta + a^2} \quad (9)$$

$$c = a\sqrt{9 + 4a^2 \sin^2 \theta} \quad (10)$$

$$\theta_1 = \cos^{-1}\left(\frac{6a^2 \cos \theta + 4a^2 \sin^2 \theta}{2a^2 \sqrt{9 + 4a^2 \sin^2 \theta}}\right) \quad (11)$$

$$\theta_2 = \cos^{-1}\left(\frac{18a^2 + 4a^2 \sin^2 \theta}{2a^2 \sqrt{90 + 40 \sin^2 \theta}}\right) \quad (12)$$

$$\theta_3 = \theta - \theta_1 - \theta_2 \quad (13)$$

$$\theta_4 = \cos^{-1}\left(\frac{2a^2 - 4a^2 \sin^2 \theta}{2a^2 \sqrt{10}}\right) \quad (14)$$

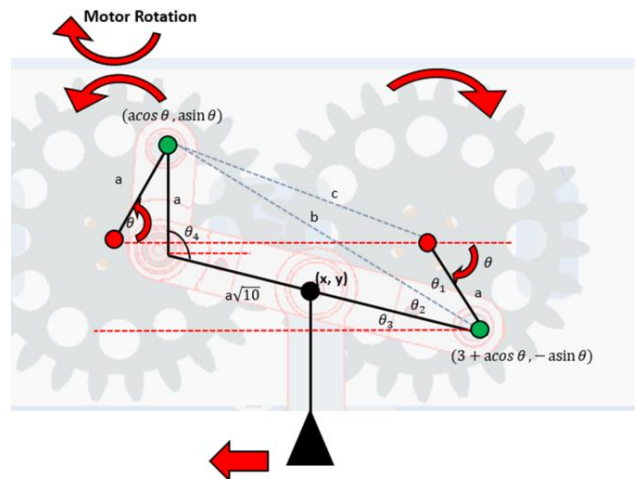


Figure 22. Each angle change according to the rotation of the gear

Depending on the rotation angle of the spur gear, the angles between the links were derived from (11~14). The driving force  $F$  is derived using these results and other forces shown in Figure 23, and its final form is determined as (18).

$$F_1 = \frac{\tau}{a} \cos(90 - \theta_1 - \theta_2 - \theta_3) \quad (15)$$

$$F_2 = T \cos(90^\circ - \theta_4 - \theta_3) \quad (16)$$

$$T = \frac{\tau}{a} \cos(\theta_4 - \theta_3 - \theta + 90^\circ) \quad (17)$$

$$F = \frac{1}{a} \left( F_1 \frac{a\sqrt{10}}{2} \sin \theta_3 + F_2 \frac{a\sqrt{10}}{2} \sin \theta_3 \right) \quad (18)$$

$T$  is the torque generated in the joint,  $F_1$  and  $F_2$  are the forces generated in the joint, and  $\tau$  is the driving motor torque. Then,  $F$  derived as in (18) is substituted into (8).

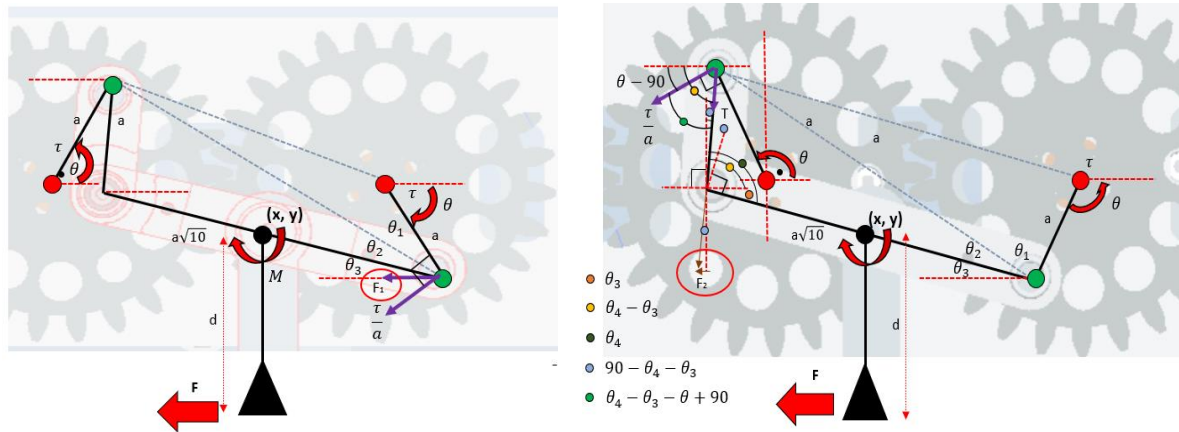


Figure 23. Geometric analysis to find the momentum

Next, since the pads of the three driving lines alternately generate and remove the vacuum pressure, it is necessary to find the vacuum pressure  $P$  applied to the pads for each movement sequence. The pressure pattern similar to the real-time pressure measured while the robot is running at 60 revolution per minute (RPM) is substituted into (5), and then into (8) again to obtain the speed of the robot. Through this pattern, it can be confirmed whether the derived (8) is appropriate.

In the top of Figure 24, we see the measured pressure of the pads of three driving lines that constitute the driving unit of the robot body while the robot moves with the driving motor rotating at 60 RPM. And the pressure pattern for a simulation is suggested as shown at the bottom of Figure 24, which is similar to the measured pressures. Then, by substituting these pressures into (8), the robot's moving speed was calculated, thus, the proposed robot's equation of motion (8) was verified by comparing the speed value calculated from the simulation with the measured value of the robot speed.

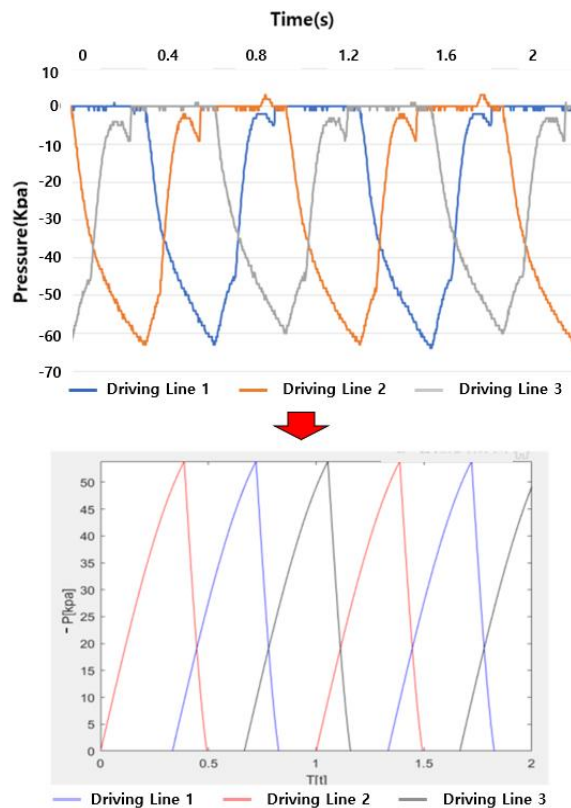


Figure 24. Pressure real measurement and analogy

Figure 24 shows the results of measuring the pressures of the three driving lines pads forming the left driving part of the robot with a pressure sensor when the robot moves forward while rotating the driving motor at 60 RPM. And the pressure patterns similar to these pressures are formed at the bottom of Figure 24. Then, by substituting these pressures and the driving force  $F$  into (8), the robot's moving speed was calculated by numerical analysis, and the proposed robot's equation of motion (8) was verified by comparing this value with the measured speed value of the robot.

The speed response driven by numerical simulation is shown in Figure 25, and to check whether the speed behavior is correct, the actual robot moving speed was measured in real time and compared with the simulation result. We measured the actual robot's moving speed by an optical flow sensor and its result is shown in Figure 26. As seen in Figure 25 and Figure 26, while the driving line pads are attached to the panel the robot is accelerated by the other two driving lines for a certain period and then the speed is reduced, thus, we see that acceleration and deceleration are repeated thrice per cycle.

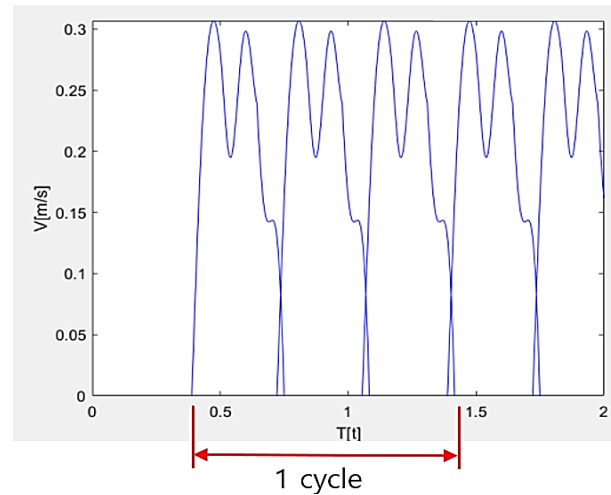


Figure 25. Simulation for robot speed response by pressure patterns on pads

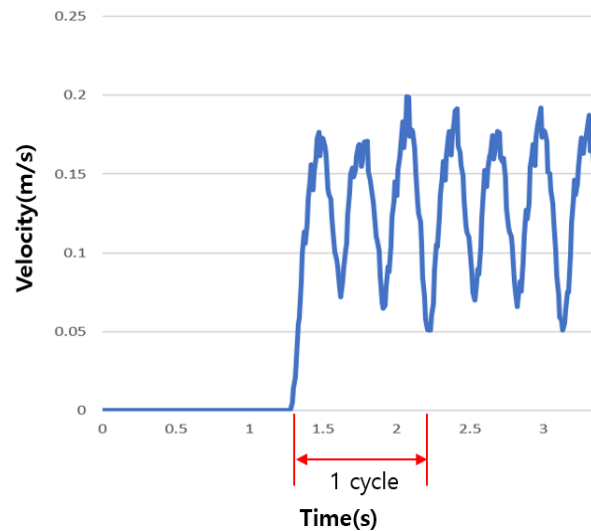


Figure 26. Measured robot-moving speed for the pressure patterns

After confirming that the acceleration/deceleration responses are similar between the simulation and the experiment, we investigated the robot's moving speed varied according to the OFF time of the solenoid valve, which affects the pressure on vacuum pads. As a result of adjusting the OFF time as shown in Figure 27, the corresponding robot's speeds were shown in Figure 28.



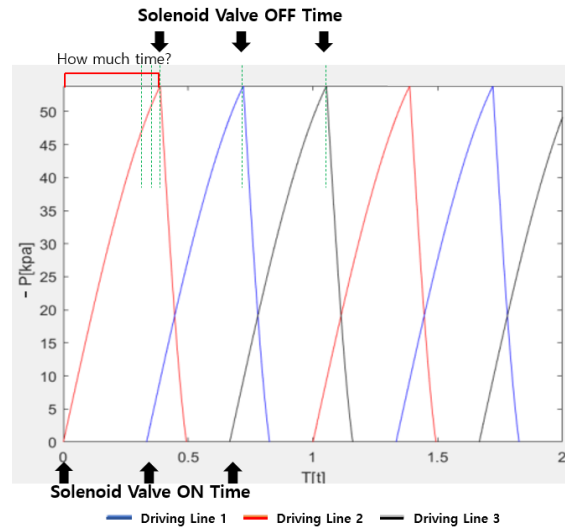


Figure 27. Solenoid valve OFF time control

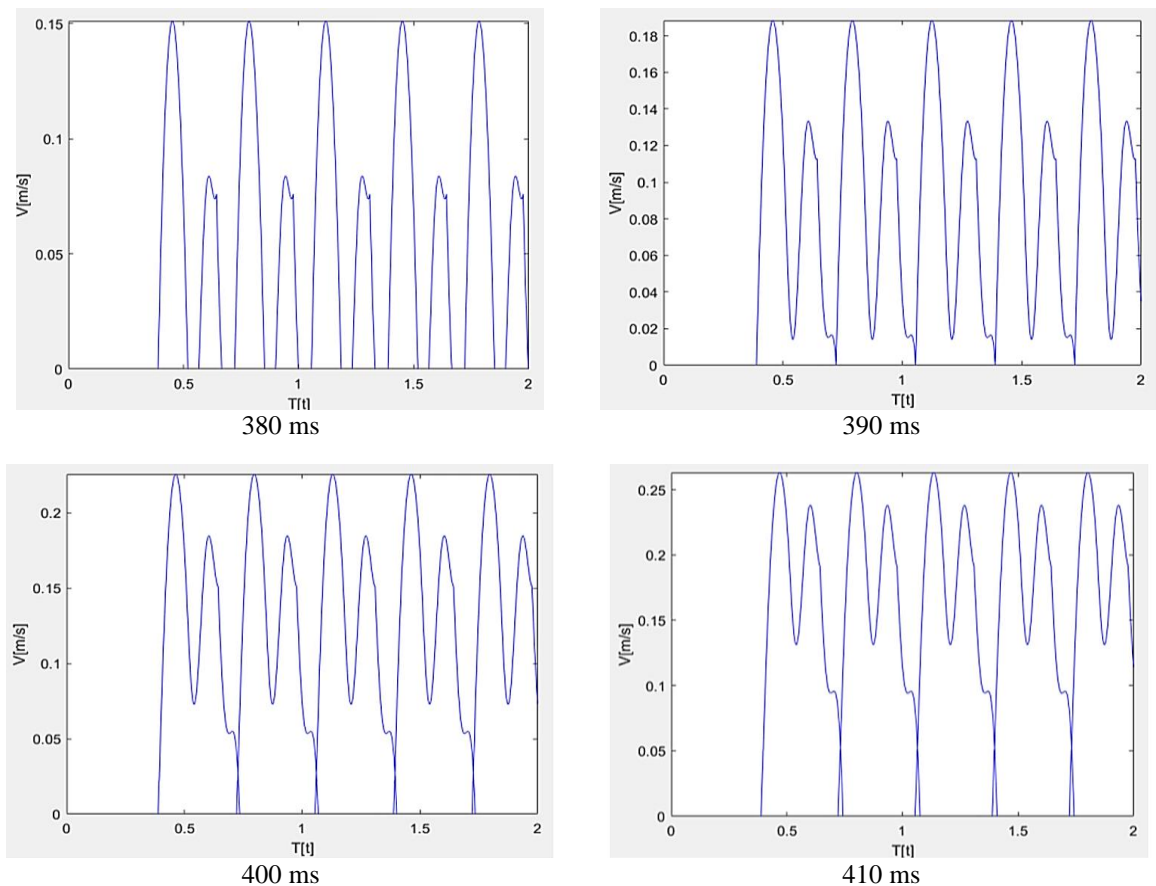


Figure 28. Robot speed behaviors according to various solenoid valve OFF time

As a result of checking the change in speed while adjusting the OFF time of each solenoid valve, the speed was the fastest in the case of 0.41 sec, but it was confirmed that the average speed was about 0.15 m/s or more. Since it deviated too much from the expected 0.1m/s, the solenoid valve OFF time running at the most ideal speed is estimated to be 0.4 seconds. By directly inputting this value, the robot moving speed was measured with the drive motor rotating 60 RPM, and compared with the actual theoretical value, and as a result, the closest result was obtained.

#### 4. EXPERIMENTAL VERIFICATION

##### 4.1. Moving test on an inclined panel

The moving speed according to the inclination angle was measured for the panel-cleaning robot with a triple driving line structure. The straight-line correction driving was also tested and measured the speed during the vertical movement of the robot up to 80 cm on the 30°, 35°, 40° and 45° inclined panels as shown in Figure 29. The results of driving on an inclined panel were summarized in Table 1. It was confirmed that the robot ascends and descends without slipping even on a 45-degree inclined panel.

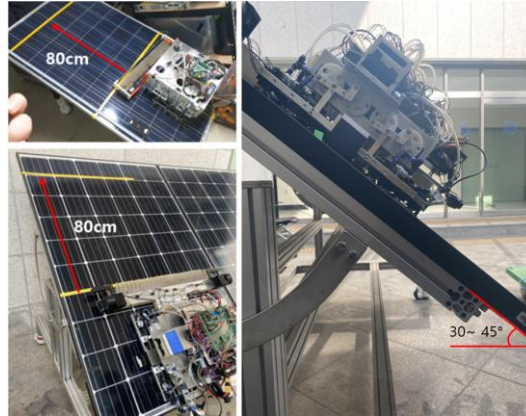


Figure 29. Robot moving speed measurement on different inclination angles

Table 1. Robot performance at each angle panel

Panel installation angle [°]	Ascending Speed [m/min]	Descending speed [m/min]
30	6.3	6.5
35	6.3	6.6
40	6.2	6.7
45	6.2	6.9

As shown in Figure 30, the degree of deviation from the reference line when the robot is driven is measured and the straightness correction is checked. The robot runs 5 times horizontally and 5 times vertically on a panel inclined at 20, 30, and 40 degrees, and the amount of distance deviating from the reference line is measured for each run and the average value is obtained. The amount of deviation from the reference line is recorded by driving 50 cm for horizontal driving and 100 cm for vertical driving. Table 2 shows the experimental results for straight-moving control for horizontal and vertical movements.

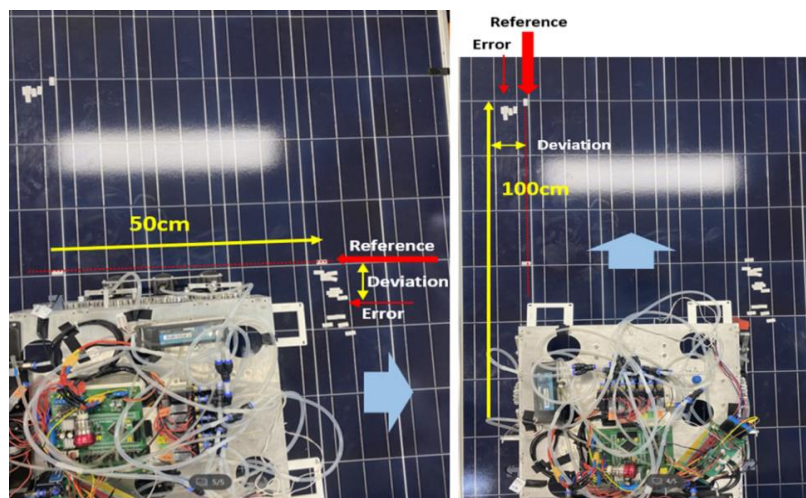


Figure 30. Experiments for straight-moving

Table 2. Driving deviation results

Panel installation angle [°]	Vertical driving		Panel installation angle [°]	Horizontal driving	
	Average deviation [mm]	Standard deviation [mm]		Average deviation [mm]	Standard deviation [mm]
20	3.0	2.24	20	4.2	1.30
30	3.2	1.92	30	5.4	1.14
40	4.4	0.89	40	9.8	3.11

In the case of vertical driving, the deviation value was measured to be 3 mm or less. Since the legs of the robot have a triple driving line structure, the motors that drive both legs can be controlled separately, so a straight-line correction control is possible. And in the case of horizontal driving, the gap between the driving lines is minimized by installing straight-line compensation and driving guides to reduce slippage during movement. Figure 31 shows the straight-line driving, rotation, and crossing over a gap between inclined panels.

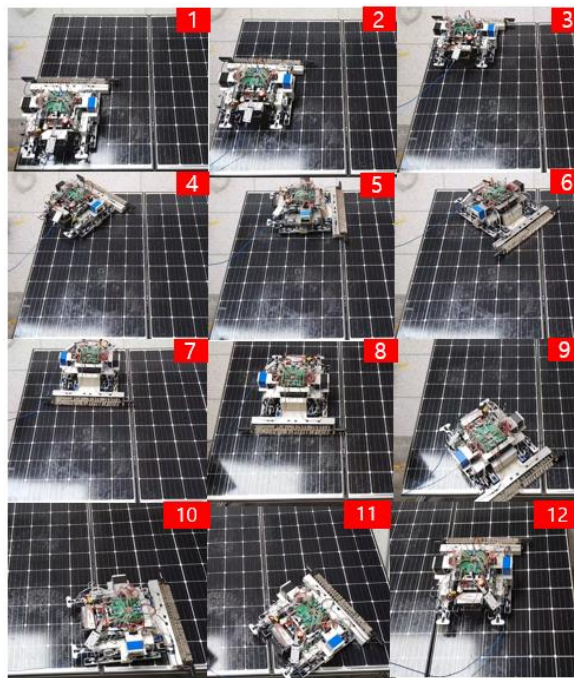


Figure 31. Robot motion of straight-line driving, rotation, and crossing over a gap between panels

#### 4.2. Performance test for solenoid valve OFF time adjustment

Next, the speed of the robot was measured while changing the solenoid valve OFF time and compared with the theoretically calculated value to verify whether stable driving was performed. The experimental environment and method are. The solenoid valve OFF time is input to the controller. While the motor driving both legs of the robot rotated at 60 RPM, the robot moved 100 cm vertically on the 40 degree inclination solar panel, and we measured the robot's moving speed. When the driving motor rotates at 60 RPM in the manufactured robot, it moves 105 mm per cycle consisting of a sequence of three driving lines, which results in a robot speed of 10.5 cm/s. Comparing this theoretical value with the actual speed value, the traveling speed was measured three times for each OFF time of the solenoid valve, and the average value was obtained.

As a result of the experiments in Table 3, all cases were smaller than the theoretical value of 10.5 cm/s. However, when the solenoid valve OFF time was 0.4 to 0.41 sec, it became the fastest speed. There was no significant difference in moving speed in each case, but when the solenoid valve was turned OFF at 0.38 and 0.39 seconds, it was found that the robot had a relatively slow speed. It is estimated that the speed was measured slowly because the driving line pads attached first released the vacuum pressure a little faster before the adjacent driving line pads were attached to the panel. Figure 32 shows the results of measuring the pad pressure of each driving line in real time while driving. First of all, it is expected that some

pressure leakage has occurred because the vacuum pressure created by the three driving lines is not constant. It was found useful to use this motion analysis to find the most optimal solenoid valve OFF time.

Table 3. Measurement of running speed according to the solenoid valve OFF times (Unit: cm/s)

Solenoid valve OFF time (ms)	1 <sup>st</sup>	2 <sup>nd</sup>	3 <sup>rd</sup>	Average
380	10.35	10.25	10.31	10.30
390	10.31	10.33	10.39	10.34
400	10.36	10.42	10.48	10.42
410	10.42	10.45	10.40	10.42

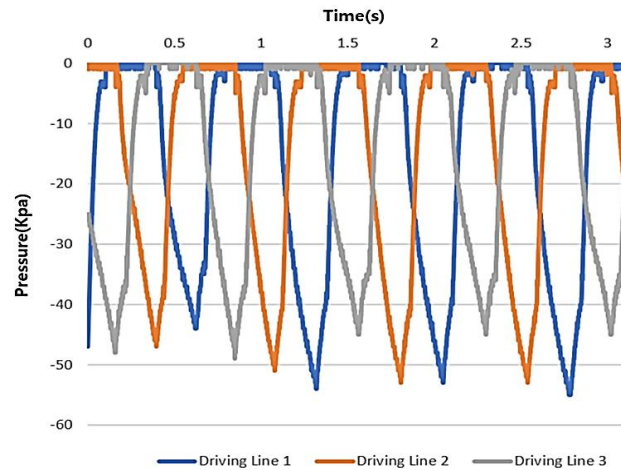


Figure 32. Real-time pressure measurement while driving the robot

## 5. CONCLUSION

In this study, we dealt with the development of the driving mechanism of the solar panel-cleaning robot to clean the solar panel at a 40-degree inclination. A driving unit composed of triple driving lines was proposed and applied to the robot, enabling the robot to move in the form of walking parallel to the panel. A driving unit composed of triple driving lines was proposed and applied to the robot, enabling the robot to move in the form of walking parallel to the panel. By introducing a link mechanism to the driving line, the vertical movement of the robot was minimized, thereby reducing the vibration of the sensor and camera mounted on the robot.

A robot equipped with 3 driving lines per driving unit was manufactured and the performance was evaluated through driving tests. As a result of the driving tests of the manufactured robot, driving was possible up to a maximum panel inclination of 45 degrees, and it was possible to drive at a maximum speed of 6.3 m/min. By installing a guide between the driving lines, the gap between the links is minimized, so there is very small slippage in horizontal driving on the panel. By adopting the triple driving lines, it was possible to increase the moving speed of the robot by continuously attaching and detaching from the panel. With this driving unit configuration, which enables individual control of the drive motors, straight line-driving became possible. However, since the number of mechanical parts increased by having three driving lines, the weight of the robot increased compared to the double driving line structure, so the driving motor torque was increased to drive the robot on a panel with a higher inclination angle, and 24 pads were installed. A total of 30 pads were used by adding 6 for the rotation module.

By adjusting the appropriate solenoid valve OFF time, the robot can run stably and at the optimum speed. By controlling the adsorption and desorption of the pads by the OFF time of the valve, the speed of the robot could be controlled. Through motion analysis, it was possible to find an appropriate solenoid valve OFF time for stable driving. Also, when parameters such as the weight or link length of the robot are changed, the optimum driving conditions are met by adjusting the appropriate solenoid valve OFF time.

## ACKNOWLEDGMENTS

This research was supported by Korea Evaluation Institute of Industrial Technology grant funded by the Korea Government (MOTIE) (P2004321) and by Korea Institute for Advancement of Technology (KIAT) grant funded by the Korea Government(MOTIE) (P0008473, HRD Program for Industrial Innovation).







## REFERENCES

- [1] J. H. Kang, "Solar industry report Q3 2019," 2019.
- [2] J. H. Kang, "Solar industry report Q1 2019," 2019.
- [3] T. Gerarden, "Demanding innovation the impact of consumer subsidies on solar panel production costs," *Manuscript, Dyson School of Applied Economics and Management, Cornell University*, 2018.
- [4] D. H. Kim, "Global PV market prospect and response plan of the Korean PV industry," *Bulletin of the Korea Photovoltaic Society*, vol. 79–82, 2015.
- [5] M. nmas G. N. Grando, E. R. Maletz, D. Martins, H. Simas, and R. Simoni, "Robots for cleaning photovoltaic panels: state of the art and future prospects," *Revista Tecnología y Ciencia*, no. 35, pp. 137–150, May 2019, doi: 10.33414/rtyc.35.137-150.2019.
- [6] Ö. Akyazi, E. Şahin, T. Özsoy, and M. Algül, "A solar panel cleaning robot design and application," *European Journal of Science and Technology*, pp. 343–348, Oct. 2019, doi: 10.31590/ejosat.638291.
- [7] S. Parashar and R. Parashar, "Artificial intelligence in robotic cleaners-a new revolutionary paradigm for India's most ambitious solar energy program," in *2018 5th International Conference on "Computing for Sustainable Global Development"*, 2018, pp. 4924–4928.
- [8] G. Anilkumar *et al.*, "Design and development of wireless networking for solar PV panel cleaning robots," *IOP Conference Series: Materials Science and Engineering*, vol. 937, no. 1, Sep. 2020, doi: 10.1088/1757-899X/937/1/012024.
- [9] M. Sundaram, S. Prabhakaran, T. Jishnu, and S. Sharma, "Design and analysis of an autonomous cleaning robot for large scale solar PV farms," in *Automatic Control, Mechatronics and Industrial Engineering*, CRC Press, 2019, pp. 265–272. doi: 10.1201/9780429468605-37.
- [10] H. K. Kim, "Green building photovoltaic installation guide," *Green Planning Group Cheongyeon*, 2017.
- [11] C. H. Moon, "A study on the building design guideline development considering photovoltaic panel installation," *Journal of the Regional Association of Architectural Institute of Korea*, pp. 139–146, 2019.
- [12] N. Hashim, M. N. Mohammed, R. AL Selvarajan, S. Al-Zubaidi, and S. Mohammed, "Study on solar panel cleaning robot," in *2019 IEEE International Conference on Automatic Control and Intelligent Systems (I2CACIS)*, Jun. 2019, pp. 56–61. doi: 10.1109/I2CACIS.2019.8825028.
- [13] N. Ronnaronglit and N. Maneerat, "A cleaning robot for solar panels," in *2019 5th International Conference on Engineering, Applied Sciences and Technology (ICEAST)*, Jul. 2019, pp. 1–4. doi: 10.1109/ICEAST.2019.8802521.
- [14] T. Sorndach, N. Pudchuen, and P. Srisungsithisunti, "Rooftop solar panel cleaning robot using omni wheels," in *2018 2nd International Conference on Engineering Innovation (ICEI)*, Jul. 2018, pp. 7–12. doi: 10.1109/ICEI18.2018.8448530.
- [15] M. U. Hassan, M. I. Nawaz, and J. Iqbal, "Towards autonomous cleaning of photovoltaic modules: Design and realization of a robotic cleaner," in *2017 First International Conference on Latest trends in Electrical Engineering and Computing Technologies (INTELLECT)*, Nov. 2017, pp. 1–6. doi: 10.1109/INTELLECT.2017.8277631.
- [16] Z. Houxiang, Z. Jianwei, and Z. Guanghua, "Requirements of glass cleaning and development of climbing robot systems," in *2004 International Conference on Intelligent Mechatronics and Automation, 2004. Proceedings*, 2004, pp. 101–106. doi: 10.1109/ICIMA.2004.1384170.
- [17] T. Miyake, H. Ishihara, R. Shoji, and S. Yoshida, "Development of small-size window cleaning robot by wall climbing mechanism," Oct. 2006. doi: 10.22260/ISARC2006/0042.
- [18] H. Kim, K.-C. Seo, J.-W. Kim, and H.-S. Kim, "Design of tracked wheel mechanism for wall climbing robot," in *Proceedings of the Korean Society of Precision Engineering Conference*, 2010, pp. 215–216.
- [19] M. I. Seo, M. H. Kim, J. H. Kim, and D. H. Kim, "Autonomous driving system design of solar panel cleaning robot using vacuum adsorption mechanism," *Transactions of the Korean Society of Mechanical Engineers-A*, vol. 44, no. 8, pp. 569–579, Aug. 2020, doi: 10.3795/KSME-A.2020.44.8.569.
- [20] Y. Yoshida and S. Ma, "A wall-climbing robot without any active suction mechanisms," in *2011 IEEE International Conference on Robotics and Biomimetics*, Dec. 2011, pp. 2014–2019. doi: 10.1109/ROBIO.2011.6181587.
- [21] H. Kim *et al.*, "Development of a wall climbing robot with vacuum caterpillar wheel system," in *Proceedings of the Korean Society of Precision Engineering Conference*, 2006, pp. 55–56.
- [22] H.-J. Kim, Y. Jeong, J.-W. Kim, and T.-J. Nam, "M. Sketch," in *Proceedings of the 29th Annual Symposium on User Interface Software and Technology*, Oct. 2016, pp. 75–77. doi: 10.1145/2984751.2985709.
- [23] "RecurDyn support," *FunctionBay Ltd.* <https://support.functionbay.com/en/page/single/16/professional> (accessed Sep. 13, 2020).
- [24] V. Korendiy, "Analysis of structure and kinematics of four-bar crank-rocker walking mechanism," *Ukrainian journal of mechanical engineering and materials science*, pp. 21–34, 2015.
- [25] A. Ghassaei, P. P. Choi, and D. Whitaker, "The design and optimization of a crank-based leg mechanism," *Pomona, USA*, 2011.
- [26] W. J. Jang, J. G. Kim, Y. I. Han, P. D. G., and K. D. H., "Typed solar panel cleaning robot using triple driving mechanism with vacuum pads," in *The Korean Society of Mechanical Engineers Spring Conference 2020*, 2020, pp. 11–12.





## BIOGRAPHIES OF AUTHORS







**Woo Jin Jang**     received the M.S. degrees in Seoul National University of Technology (2021). His master thesis focuses on the Robotics, Mechanism Analysis. Currently, He is working as a Researcher in SAMSUNG Electronics Co., Ltd. Korea. He can be contacted at [jw122016@naver.com](mailto:jw122016@naver.com).









**Jin Gahk Kim**     received B.S. degrees in Seoul National University (2020). He is currently a graduate student in Seoul National University of Technology. His research interests include Robotics, Mechatronics, and automation system development. He can be contacted at [jingahk2@naver.com](mailto:jingahk2@naver.com).



**Sang Hun Lee**     is currently a student in Seoul National University of Technology. He is currently an undergraduate student in Robot Nano Control Laboratory in Seoul National University of Technology. His research interests are mechatronics, robot vision system, robotics system, and embedded software. He can be contacted at [oklsh918@naver.com](mailto:oklsh918@naver.com).



**Dong Hwan Kim**     received B.S and M.S from Department of Mechanical Design and Production Engineering at Seoul National University in 1986 and 1988. Also he received Ph.D. from Georgia Institute of Technology, USA. He worked at Korea Institute of Industrial Technology from 1997-1998. He joined Seoul National University of Science and Technology in 1998 as professor at Department of Mechanical System Design Engineering. His major research interests are robot control, deep learning, and mechatronics. He is doing numerous projects on robot mechanism and control, artificial intelligence applications to robot, and smart mechatronics system. He can be contacted at [dhkim@seoultech.ac.kr](mailto:dhkim@seoultech.ac.kr).